

B. Friedman,^{1,*} T.A. Carter,¹ M.V. Umansky,² D. Schaffner,¹ and B. Dudson³

¹*Department of Physics and Astronomy, University of California, Los Angeles, California 90095-1547, USA*

²*Lawrence Livermore National Laboratory, Livermore, California 94550, USA*

³*Department of Physics, University of York, Heslington, York YO10 5DD, United Kingdom*

Energy dynamics calculations in a 3D fluid simulation of drift wave turbulence in the linear Large Plasma Device (LAPD) [W. Geikelman *et al.*, Rev. Sci. Instr. **62**, 2875 (1991)] illuminate processes that drive and dissipate the turbulence. These calculations reveal that a nonlinear instability dominates the injection of energy into the turbulence by overtaking the linear drift wave instability that dominates when fluctuations about the equilibrium are small. The nonlinear instability drives flute-like ($k_{\parallel} = 0$) density fluctuations using free energy from the background density gradient. Through nonlinear axial wavenumber transfer to $k_{\parallel} \neq 0$ fluctuations, the nonlinear instability accesses the adiabatic response, which provides the requisite energy transfer channel from density to potential fluctuations as well as the phase shift that causes instability. The turbulence characteristics in the simulations agree remarkably well with experiment. When the nonlinear instability is artificially removed from the system through suppressing $k_{\parallel} = 0$ modes, the turbulence develops a coherent frequency spectrum which is inconsistent with experimental data.

PACS numbers:

I. INTRODUCTION

It is common practice to study a system's linear stability properties to gain insight into turbulent dynamics. It is often easier to calculate and analyze linear modes and growth rates than to simulate and analyze nonlinear turbulence. However, there are several situations in which linear properties can be misleading in understanding turbulent systems. First, linear studies of magnetically confined plasmas that neglect stable branches of the linear dispersion relation often miss details of nonlinear dynamics. For example, stable eigenmodes can often impact nonlinear dynamics by providing energy sinks and sometimes energy sources not found on the most unstable linear branch [1–10]. Stable eigenmodes can shift the energy injection and dissipation ranges, making the turbulent dynamics very different from the Kolmogorov picture of hydrodynamic turbulence [11]. Second, systems with non-normal modes (non-orthogonal eigenvectors) display properties that are unexpected from linear calculations [12]. In fact, systems with non-normal modes even make it difficult to predict dynamics when stable eigenmode branches are included in analyses [8]. Third, linear stability analysis can miss crucial nonlinear instability effects, which come in several varieties.

The most obvious variety of a nonlinear instability effect is that of subcritical turbulence in which no linear instabilities exist but turbulence is self-sustained given finite-amplitude seed perturbations. Subcritical turbulence is common in hydrodynamics [13]. While not as well-known in plasma physics, several cases of subcritical plasma instabilities have been shown in the literature [14–20]. The second variety of nonlinear instability includes cases in which a particular linear instability is present in a system, but the turbulence is maintained by a nonlinear instability mechanism with different physical origin than the linear instability mechanism. This has been explored in tokamak edge simulations in which linear ballooning instability drive is overtaken in the saturated phase by a nonlinear drift-wave drive [21–25]. Finally, it is often found that a particular linear instability is enhanced, depressed, and/or modified in the saturated phase by a nonlinear instability with a similar mechanism as the linear instability. In some of these cases nonlinear wavenumber transfers can increase or cause drive [26, 27], while in other cases zonal flow effects decrease drive [28, 29].

In order to avoid the pitfalls of relying too heavily on linear stability calculations in forming conclusions on turbulence characteristics, it is useful to perform turbulent simulations and diagnose them with energy dynamics analyses. Energy dynamics analyses track energy input into turbulent fluctuations and energy dissipation out of them. They also track conservative energy transfer between different energy types (e.g. from potential to kinetic energy) and between different scales, waves, or eigenmodes of a system. In all, energy dynamics analysis can be used as a post-processing tool to characterize simulation turbulence in order to gain insight into underlying physical processes.

In this study, a simulation of a two-fluid Braginskii model of turbulence in the Large Plasma Device (LAPD) is subjected to such an energy dynamics analysis. This reveals that a nonlinear instability drives and maintains

*Electronic address: friedman@physics.ucla.edu

the turbulence in the steady state saturated phase of the simulation. While a linear resistive drift wave instability resides in the system, the nonlinear drift wave instability dominates when the fluctuation amplitude becomes large enough. The primary linear instability is the resistive drift wave which has a positive linear growth rate for low but finite k_{\parallel} . However, the saturated state of the simulated turbulence is strongly dominated by flute-like ($k_{\parallel} = 0$) fluctuations in density and potential. The flute-like fluctuation spectrum is generated by a nonlinear instability. The nonlinear instability is identified by its energy growth rate spectrum, which varies significantly from the linear growth rate spectrum. If $k_{\parallel} = 0$ fluctuations are removed from the simulation (while retaining zonal flows), the saturated turbulent state is qualitatively and quantitatively different and much less consistent with experimental measurement.

II. THE DRIFT WAVE MODEL

A Braginskii-based fluid model [30] is used to simulate drift wave turbulence in LAPD using the BOUT++ code [31]. The evolved variables in the model are the plasma density, N , the electron fluid parallel velocity $v_{\parallel e}$, the potential vorticity $\varpi \equiv \nabla_{\perp} \cdot (N_0 \nabla_{\perp} \phi)$, and the electron temperature T_e . The ions are assumed cold in the model ($T_i = 0$), which eliminates ion temperature gradient drive, and sound wave effects are neglected. Details of the simulation code and derivations of the model may be found in previous LAPD verification and validation studies [32–35], although electron temperature fluctuations were not included in those studies.

The equations are developed with Bohm normalizations: lengths are normalized to the ion sound gyroradius ρ_s , times to the ion cyclotron time ω_{ci}^{-1} , velocities to the sound speed c_s , densities to the equilibrium peak density, and electron temperatures and potentials to the equilibrium peak electron temperature. All of these values are constants (not functions of radius) and the physical quantities used to calculate these constants are the following: the magnetic field is 1 kG, the ion unit mass is 4, the peak density is $2.86 \times 10^{12} \text{ cm}^{-3}$, and the peak electron temperature is 6 eV. The equations are:

$$\partial_t N = -\mathbf{v}_E \cdot \nabla N_0 - N_0 \nabla_{\parallel} v_{\parallel e} + \mu_N \nabla_{\perp}^2 N + S_N + \{\phi, N\}, \quad (1)$$

$$\partial_t v_{\parallel e} = -\frac{m_i}{m_e} \frac{T_{e0}}{N_0} \nabla_{\parallel} N + \frac{m_i}{m_e} \nabla_{\parallel} \phi - \nu_e v_{\parallel e} + \{\phi, v_{\parallel e}\}, \quad (2)$$

$$\partial_t \varpi = -N_0 \nabla_{\parallel} v_{\parallel e} - \nu_{in} \varpi + \mu_{\phi} \nabla_{\perp}^2 \varpi + \{\phi, \varpi\}, \quad (3)$$

$$\begin{aligned} \partial_t T_e = & -\mathbf{v}_E \cdot \nabla T_{e0} - 1.71 \frac{2}{3} T_{e0} \nabla_{\parallel} v_{\parallel e} + \frac{2}{3 N_0} \kappa_{\parallel e} \nabla_{\parallel}^2 T_e \\ & - \frac{2 m_e}{m_i} \nu_e T_e + \mu_T \nabla_{\perp}^2 T_e + S_T + \{\phi, T_e\}. \end{aligned} \quad (4)$$

In these equations, μ_N , μ_T , and μ_{ϕ} are artificial diffusion and viscosity coefficients used for sub-grid dissipation. They are large enough to allow saturation and grid convergence [35], but small enough to allow for turbulence to develop. In the simulations, they are all given the same value of 1.25×10^{-3} in Bohm-normalized units. This is the only free parameter in the simulations. All other parameters such as the electron collisionality ν_e , ion-neutral collisionality ν_{in} , parallel electron thermal conductivity $\kappa_{\parallel e}$, and mass ratio $\frac{m_i}{m_e}$ are calculated from the experimental parameters. There are two sources of free energy: the density gradient due to the equilibrium density profile N_0 , and the equilibrium electron temperature gradient in T_{e0} , both of which are taken from experimental fits. N_0 and T_{e0} are functions of only the radial cylindrical coordinate r , and they are shown in Fig. 1.

The terms in Poisson brackets are the $E \times B$ advective nonlinearities, which are the only nonlinearities used in the simulations. The numerical simulations are fully spatial in all three dimensions (as opposed to spectral) and use cylindrical annular geometry ($12 < r < 40 \text{ cm}$). The simulations use periodic boundary conditions in the axial (z) direction and Dirichlet boundary conditions in the radial (r) direction for the fluctuating quantities.

Simulations also use density and temperature sources (S_n and S_T) in order to keep the equilibrium profiles from relaxing away from their experimental shapes. These sources subtract out the azimuthal averages ($m = 0$ component of the density and temperature fluctuations) at each time step. The azimuthal average of the potential ϕ is allowed to evolve in the simulation, allowing zonal flows to arise. The parallel current, which is often found explicitly in these equations is replaced here by $J_{\parallel} = -N_0 v_{\parallel e}$.

Some basic statistical properties of the density fluctuations of the simulation are shown in Fig. 2 and are compared to the corresponding results from the experiment on which this simulation is based. The simulation reproduces these characteristics of experimental measurements with rather good qualitative and quantitative accuracy.

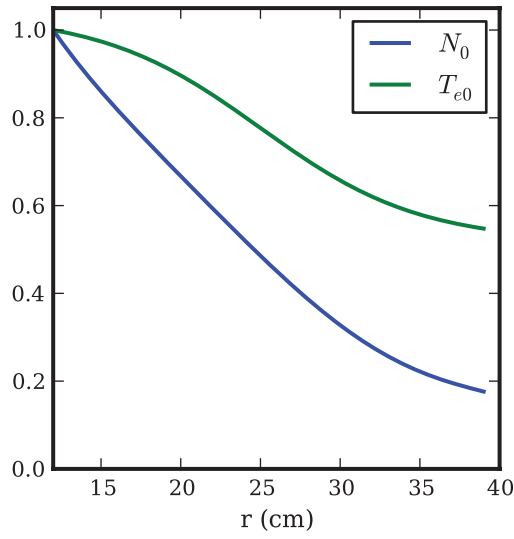


FIG. 1: The profiles of density N_0 and electron temperature T_{e0} used in the simulations normalized to their peak values of $2.86 \times 10^{12} \text{ cm}^{-3}$ and 6 eV, respectively.

III. ENERGETICS MACHINERY

In order to perform an energy dynamics analysis on the simulation, expressions for the energy and energy evolution must be derived from equations 1-4. To start, the expression for the normalized energy of the wave fluctuations in the drift wave model is:

$$E = \frac{1}{2} \int_V (N^2 + \frac{3}{2} T_e^2 + \frac{m_e}{m_i} v_{\parallel e}^2 + N_0 (\nabla_{\perp} \phi)^2) dV. \quad (5)$$

The N^2 contribution is the potential energy due to density fluctuations, $\frac{3}{2} T_e^2$ is the electron temperature fluctuation potential energy, $\frac{m_e}{m_i} v_{\parallel e}^2$ is the parallel electron kinetic energy, and $N_0 (\nabla_{\perp} \phi)^2$ is the $E \times B$ perpendicular kinetic energy. These energies are defined in this way so that they are conserved individually by their respective advective nonlinearities, although they are physically relevant as well.

Now, it is most instructive to analyze the spectral energy dynamics rather than the total energy dynamics. To do this, each fluid field ($N, T_e, v_{\parallel e}, \phi$) at a given time is Fourier decomposed as $F(r, \theta, z) = \sum_{\vec{k}} f_{\vec{k}}(r) e^{i(m\theta + k_z z)}$, where the subscript \vec{k} represents the spectral wavenumbers, (m, n) . m is the azimuthal wavenumber while n is the axial integer wavenumber such that $k_z \equiv k_{\parallel} = 2\pi n / l_z$. Note that the radial direction is not spectrally decomposed because the radial dependence of the profiles and differential operators complicates the analysis. With this, the energy of each Fourier $\vec{k} = (m, n)$ mode is

$$E_{tot}(\vec{k}) = \frac{1}{2} \left\langle |n_{\vec{k}}|^2 + \frac{3}{2} |t_{\vec{k}}|^2 + \frac{m_e}{m_i} |v_{\vec{k}}|^2 + N_0 \left| \frac{\partial \phi_{\vec{k}}}{\partial r} \right|^2 + N_0 \frac{m^2}{r^2} |\phi_{\vec{k}}|^2 \right\rangle, \quad (6)$$

where the brackets $\langle \rangle$ represent the radial integral: $\int_{r_a}^{r_b} r dr$. The energy evolution for each Fourier mode of each field has the form:

$$\frac{\partial E_j(\vec{k})}{\partial t} = Q_j(\vec{k}) + C_j(\vec{k}) + D_j(\vec{k}) + \sum_{\vec{k}'} T_j(\vec{k}, \vec{k}'). \quad (7)$$

The index j stands for each field, (n, t, v, ϕ) , and the sum over j gives the total energy evolution. Note that with the conventions used, the symbol n denotes both the axial mode number as well as the Fourier coefficient of the density fluctuation. The differences should be clear in context. The derivation of equation 7 is given in the Appendix along with the full expressions for each of the parts. $T_j(\vec{k}, \vec{k}')$ is the nonlinear energy transfer function

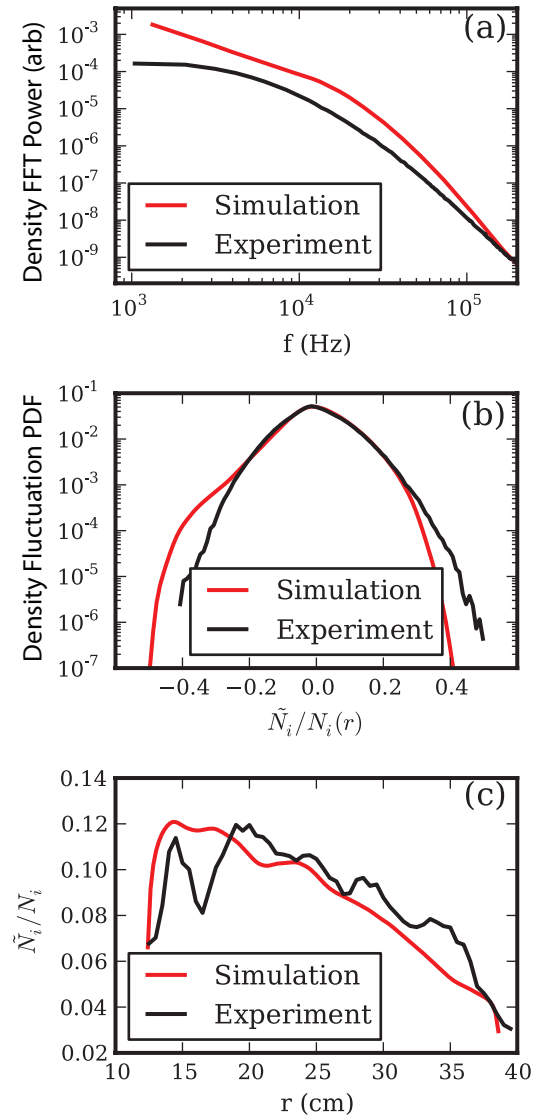


FIG. 2: **a)** The power spectral density of the density fluctuations, showing the results from simulation versus experiment, **b)** the probability distribution function of the density fluctuations, and **c)** the RMS amplitude of the density fluctuations as a function of radius.

that comes from the advective nonlinearities. It describes the nonlinear energy transfer rate of modes $\vec{k}' = (m', n')$ and $\vec{k} - \vec{k}' = (m - m', n - n')$ to the mode $\vec{k} = (m, n)$. In other words, a positive value of $T_j(\vec{k}, \vec{k}')$ indicates that fluctuations at wavenumber \vec{k} gain energy from gradient fluctuations at wavenumber \vec{k}' and flow fluctuations at wavenumber $\vec{k} - \vec{k}'$. When summed over \vec{k}' as in equation 7, the result is the total nonlinear energy transfer into mode \vec{k} . Note that $\sum_{\vec{k}, \vec{k}'} T_j(\vec{k}, \vec{k}') = 0$ because the nonlinearities conserve energy individually in each of equations 1-4. This is easily proven by the following identity:

$$\int_{\Omega} q\{p, q\} d\Omega = \int_{\Omega} p\{p, q\} d\Omega = 0, \quad (8)$$

which holds when boundary conditions are periodic or zero value as they are in the simulation. The fact that the advective nonlinearities conserve energy means that they can transfer energy between different Fourier modes but they cannot change the energy of the volume-averaged fluctuations as a whole. Only the linear terms can change the total energy of the fluctuations. Other possible nonlinearities that do not conserve energy are not included in the model equation set or in the simulations for simplicity of the energy analysis. Furthermore, it is convenient for the simulations to employ an energy conserving finite difference scheme for the advective nonlinearities to reflect this

analytic property of the equations. However, most common numerical advection schemes do not conserve energy for finite grid spacing. Therefore, an Arakawa advection scheme [36] that conserves energy of the advected quantity is used for the nonlinear advection terms in the simulations.

The linear terms in equations 1-4 do not conserve energy individually or as a whole. The linear terms are broken up into three contributions in Eqn. 7. $D_j(\vec{k})$ represents nonconservative energy dissipation due to collisions, artificial diffusion and viscosity, and the purely dissipative density and temperature sources. Each contribution to $D_j(\vec{k})$ is negative, and the exact expressions are given in the Appendix. $C_j(\vec{k})$ contains the linear terms dubbed “transfer channels” [23]. They are rewritten here:

$$C_n(\vec{k}) = \text{Re} \left\{ \left\langle -ik_z N_0 v_{\vec{k}} n_{\vec{k}}^* \right\rangle \right\} \quad (9)$$

$$C_v(\vec{k}) = \text{Re} \left\{ \left\langle -ik_z N_0 n_{\vec{k}} v_{\vec{k}}^* + ik_z N_0 \phi_{\vec{k}} v_{\vec{k}}^* - 1.71 ik_z T_{e0} t_{\vec{k}} v_{\vec{k}}^* \right\rangle \right\} \quad (10)$$

$$C_\phi(\vec{k}) = \text{Re} \left\{ \left\langle ik_z N_0 v_{\vec{k}} \phi_{\vec{k}}^* \right\rangle \right\} \quad (11)$$

$$C_t(\vec{k}) = \text{Re} \left\{ \left\langle -1.71 ik_z T_{e0} v_{\vec{k}} t_{\vec{k}}^* \right\rangle \right\} \quad (12)$$

Notice that $C_n(\vec{k}) + C_v(\vec{k}) + C_\phi(\vec{k}) + C_t(\vec{k}) = 0$, which is most clearly seen upon conjugation of $C_v(\vec{k})$ inside the real part operator. This is the reason why these terms are called transfer channels. They represent the transfer between the different types of energy of the different fields ($N, \phi, T_e \leftrightarrow v_{\parallel e}$), but taken together, they do not create or dissipate total energy from the system. The only energy field transfer in this system occurs through the parallel electron velocity (parallel current) dynamics. There is no direct transfer between the state variables N, ϕ , and T_e . Altogether, the coupling through the parallel current is called the adiabatic response. It is an essential part of both the linear and nonlinear drift wave mechanisms [23, 25]. The adiabatic response moves energy from the pressure fluctuations to the perpendicular flow through the parallel current.

Finally, the $Q_j(\vec{k})$ terms represent the nonconservative energy sources. They are rewritten here:

$$Q_n(\vec{k}) = \text{Re} \left\{ \left\langle -\frac{im}{r} \partial_r N_0 \phi_{\vec{k}} n_{\vec{k}}^* \right\rangle \right\} \quad (13)$$

$$Q_v(\vec{k}) = \text{Re} \left\{ \left\langle ik_z \frac{N_0^2 - T_{e0}}{N_0} n_{\vec{k}} v_{\vec{k}}^* + ik_z (1 - N_0) \phi_{\vec{k}} v_{\vec{k}}^* + 1.71 ik_z (T_{e0} - 1) t_{\vec{k}} v_{\vec{k}}^* \right\rangle \right\} \quad (14)$$

$$Q_\phi(\vec{k}) = 0 \quad (15)$$

$$Q_t(\vec{k}) = \text{Re} \left\{ \left\langle -\frac{3im}{2r} \partial_r T_{e0} \phi_{\vec{k}} t_{\vec{k}}^* \right\rangle \right\} \quad (16)$$

$Q_n(\vec{k})$ is the energy extraction from the equilibrium density profile into the density fluctuations. This term may have either sign depending on the phase relation between $\phi_{\vec{k}}$ and $n_{\vec{k}}$, so it can in fact dissipate fluctuation potential energy from the system as well as create it at each \vec{k} . $Q_t(\vec{k})$ is completely analogous to $Q_n(\vec{k})$ but for the temperature rather than the density. $Q_v(\vec{k})$ is parallel kinetic energy extraction or dissipation, which is a rather insignificant term compared to $Q_n(\vec{k})$ and $Q_t(\vec{k})$. The sources of these terms are the equilibrium gradients, which is evident because if the profiles were flat ($N_0 = T_{e0} = 1$), all $Q(\vec{k})$ would vanish. Moreover, the particular normalization of equations 1-4 combined with the choice of energy definition (equation 5) causes the non-zero $Q_v(\vec{k})$, which again is quite insignificant.

IV. NONLINEAR ENERGY DYNAMICS

A. Energy Spectra

Figure 3 shows the time evolution of the total energy of the fluctuations. The simulation starts with a random initial perturbation, and the fluctuations grow exponentially until reaching saturation. All analysis of the saturated (turbulent) stage is done by time averaging. The turbulent spectral energy, defined in equation 6 is shown in Fig. 4. The energy is broken up into its different types (e.g. perpendicular kinetic energy: E_ϕ). There are a few clear nonlinear

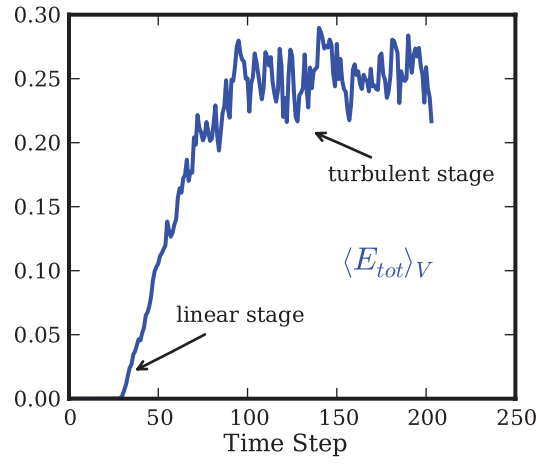


FIG. 3: Time evolution of the volume-averaged total energy. Each time step is $400/\omega_{ci} \sim 170\mu s$

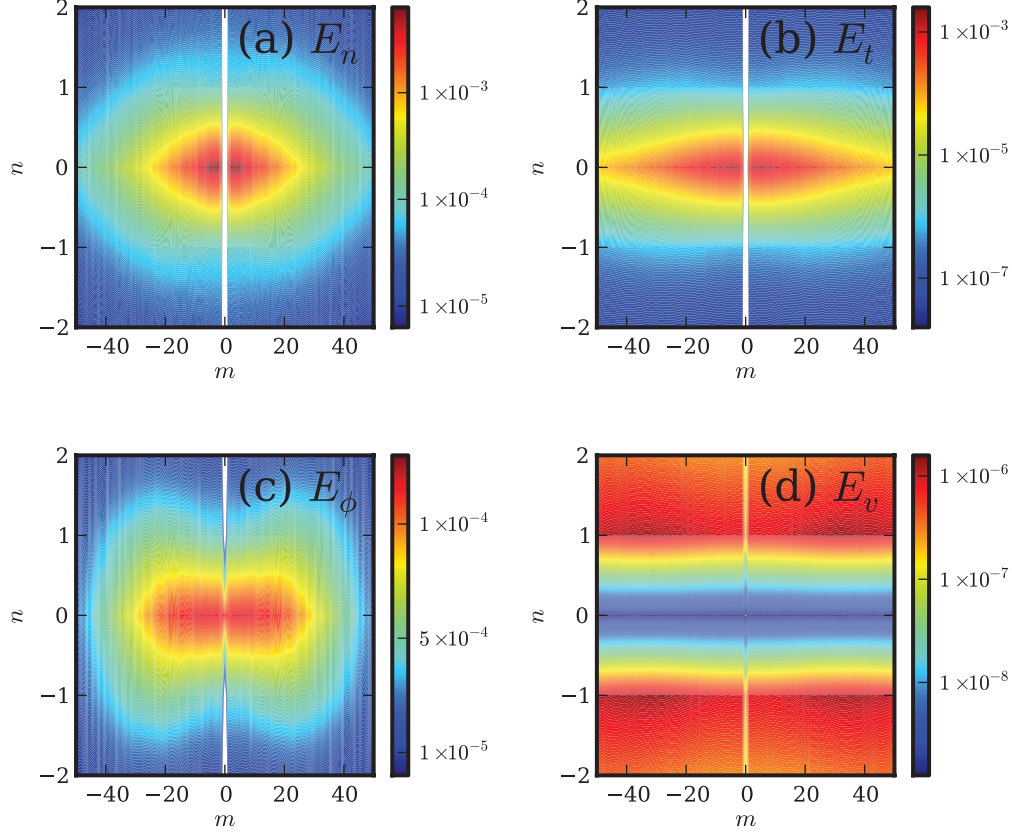


FIG. 4: **a)** $E_n(\vec{k})$, **b)** $E_t(\vec{k})$, **c)** $E_\phi(\vec{k})$, and **d)** $E_v(\vec{k})$ in the $m - n$ plane averaged over time during the saturated turbulent phase. Note the different scales used on each figure.

properties seen in these figures. The first is that the energy is located in different spectral regions for the different energy types. This has to be a nonlinear effect because the linear eigenmodes are Fourier modes in the azimuthal and axial directions and all fields grow at the same rate for an eigenmode. Another property unexpected from linear stability analysis is that most of the potential and perpendicular kinetic energy (E_n , E_t , and E_ϕ) is contained in $n = 0$ ($k_{\parallel} = 0$) structures, which are often called flute modes. Previous studies pointed out this flute mode dominance in LAPD simulations [34, 37]. One of these studies [37], however, used a momentum source that produced a large radial electric field, possibly leading to a dominating Kelvin-Helmholtz instability at $k_{\parallel} = 0$. Such a feature is unexpected in this study because there is no $n = 0$ linear instability present in the system, which is confirmed by eigenvalue

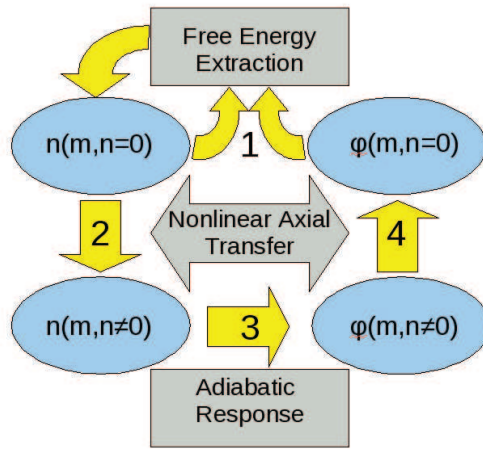


FIG. 5: Diagram of the nonlinear instability process that drives flute modes.

calculations [32]. The only linear instability of the system is the linear resistive drift wave instability, which requires finite n to provide the phase shift and state variable coupling to drive the waves unstable. Perhaps equally unexpected is the complete lack of parallel kinetic energy in the $n = 0$ range. The E_v spectrum looks like a traditional linear drift wave spectrum, but does not match the other fields, which is atypical of linear drift waves.

B. Description and Evidence for the Nonlinear Instability

The flute mode dominance has to be a nonlinear effect because linear drift waves require finite n . However, the cause of the flute dominance is not simple cascade dynamics, a secondary instability, nor a flow-driven flute-like instability such as Kelvin-Helmholtz or interchange. Rather, the cause is a primary nonlinear instability as has been reported in previous simulations of plasma edge turbulence [16, 26]. This nonlinear instability is a multi-step process that is outlined in Fig. 5. In the first step, $n = 0$ density and potential fluctuations *nonconservatively* draw energy from the equilibrium density gradient as prescribed by $Q_n(m, n = 0)$ defined in equation 13, and feed this energy into the $n = 0$ density fluctuations only. The nonconservative linear terms, after all, can only inject, dissipate, or transfer energy at one wavenumber at a time, so it takes $n = 0$ fluctuations to nonconservatively inject energy into $n = 0$ fluctuations. Note also that the temperature fluctuations work in the same way as the density fluctuations, and one could replace $n(m, n)$ (the spectral density component) with $t(m, n)$ (the spectral temperature component) in the diagram. The density and temperature are analogous and work in parallel, however the temperature fluctuations are a few times smaller than the density fluctuations and provide weaker drive because parallel heat conduction strongly dissipates the temperature fluctuations, which is why the diagram highlights the density contribution (this observation is consistent with other work in edge turbulence [22]). This nonconservative injection does not occur for infinitesimal perturbations; a finite-amplitude $n = 0$ seed perturbation is required. In the simulations, this seed is provided by nonlinear transfer from $n = 1$ drift wave fluctuations which dominate the linear phase of the turbulence simulation.

In the second step of the diagram, these $n = 0$ density fluctuations *conservatively* transfer energy to $n \neq 0$ density fluctuations by the nonlinear $T_n(\vec{k}, \vec{k}')$ transfer process. The third step involves the transfer at finite n from the density fluctuations to the potential fluctuations by way of the parallel current in the adiabatic response. The $C_j(\vec{k})$ terms describe this adiabatic response. Fourth and finally, the $T_\phi(\vec{k}, \vec{k}')$ interaction conservatively transfers energy from $n \neq 0$ to $n = 0$ potential ϕ fluctuations in inverse fashion, providing the necessary potential flute structures for the first step.

The evidence for the dominance of this mechanism is best shown with help from the energy dynamics machinery derived in section III. Figure 6 summarizes the effects of the nonconservative linear terms, which are fully responsible for injecting energy into the fluctuations. Figure 6(a) shows the E_n dynamics separated into different parallel wavenumbers and plotted against the azimuthal wavenumber m . Clearly, most of the energy is injected into $n = 0$ density structures, while only a small amount of energy is injected into $n = \pm 1$ structures despite the fact that the linear instability is active only at $n \neq 0$. The large positive $Q_n + D_n$ (injection plus dissipation) at $n = 0$ provides evidence for the first step of the diagram in Fig. 5. Note however that the dissipation from the source, which acts entirely at $m = 0$, is not shown in this figure, but is rather large. Modes with $|n| \geq 2$, on the other hand, play

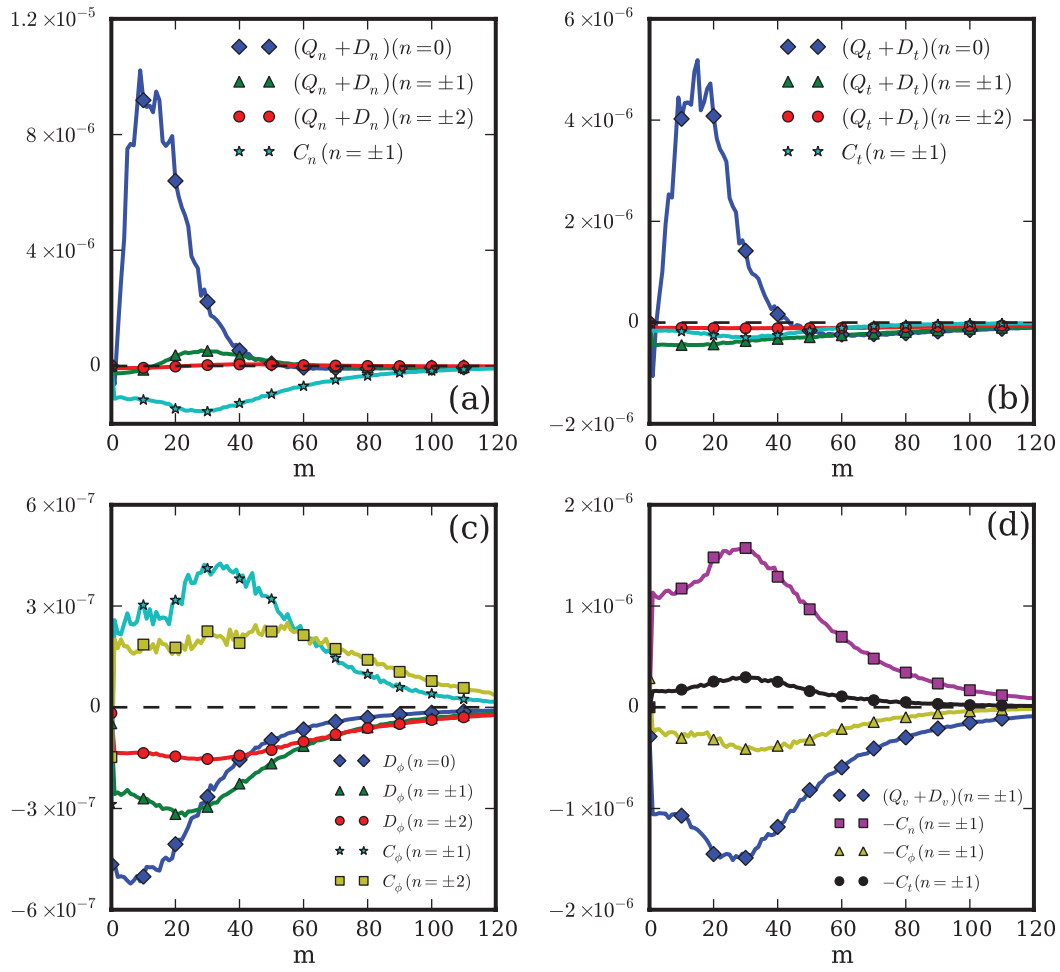


FIG. 6: **a)** The solid curves quantify the energy dynamics of the density potential energy averaged over time during the saturated turbulent phase. The notation $n \pm 1$ represents the summation over the $n = 1$ and $n = -1$ curves. **b)** The energy dynamics of the temperature potential energy, **c)** the perpendicular kinetic energy, and **d)** the parallel dynamics (adiabatic response). The contributions to $C_v(\vec{k})$ in **d)** are broken up with $C_v(\vec{k}) = -C_n(\vec{k}) - C_t(\vec{k}) - C_\phi(\vec{k})$. The density and temperature sources are neglected in **a)** and **b)** respectively. They only contribute at $m = 0$.

a negligible role in density injection, dissipation, and transfer. Furthermore, all of the net energy injected into the density fluctuations ($Q_n + D_n$) is transferred out (C_n) to the parallel current (electron velocity), which only occurs at finite n , almost entirely at $n = \pm 1$. The net change of E_n , which is the sum $Q_n + D_n + C_n$ over all m and n is approximately zero because this analysis is averaged over the steady state turbulence, although this is not so evident in Fig. 6a without the source dissipation. The necessary balance implies, as will be proven later, that the nonlinearities transfer energy from $n = 0$ to $n = \pm 1$ modes, where that energy can then be transferred to the parallel current.

Figure 6(b) shows the temperature potential energy dynamics. Again flute structures inject energy into the fluctuations, but unlike in the density case, $n = \pm 1$ modes dissipate more energy than they inject. Moreover, the small value of C_t reveals that the temperature fluctuations inject only a small amount of energy into the parallel current compared to the density fluctuations. Despite the fact that the equilibrium temperature gradient is nearly as steep as the density gradient at its steepest point, its free energy is not used efficiently by the waves in the sense that it is largely dissipated before being transferred to the electrostatic potential. The reason for the difference between the density and temperature responses is the extra dissipation routes for the temperature fluctuations, namely, the parallel heat conduction and electron-ion heat exchange. One should therefore be careful in assuming that adding free energy sources to an analysis will automatically increase instability drive. The same type of result was seen in a study of tokamak edge turbulence [22], although there, the temperature fluctuations were even more dissipative than in this study in that they actually drew energy from the parallel current.

Next, Fig. 6(c) illustrates the perpendicular kinetic energy dynamics provided by the electrostatic potential ϕ . Since there is no free energy source for the potential ($Q_\phi = 0$), the potential fluctuations derive their energy from the

parallel current through the C_ϕ transfer channel, which is positive everywhere and only finite for finite n . Otherwise, ion-neutral collisions and viscosity dissipate energy from the potential fluctuations as shown by the D_ϕ curves. An interesting detail seen in this figure is that modes with $|n| > 1$ actually contribute to the transfer channel and dissipation, whereas these modes are negligible for the other fields.

The last piece, the parallel dynamics, also called the adiabatic response, is displayed in Fig. 6(d). The primary effect of the adiabatic response is to take energy from the density fluctuations and transfer it to the potential fluctuations, which only occurs at finite parallel wavenumber. This effect corresponds to the third step in Fig. 5. Moreover, resistivity dissipates a substantial portion of this parallel kinetic energy and, although not evident from this figure, provides the primary phase shift mechanism between the density and potential that allows for instability. The temperature fluctuations also provide energy to the potential fluctuations through this response, although it is much weaker than the density fluctuation route.

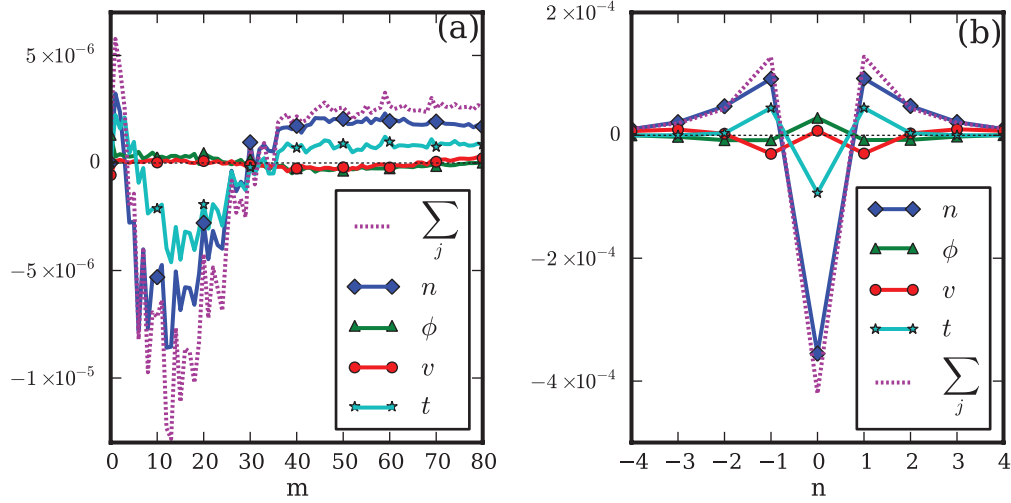


FIG. 7: **a)** Conservative nonlinear energy transfer functions $T_j(\vec{k}, \vec{k}')$ summed over \vec{k}' and n . The line labeled ϕ represents the function $\sum_{\vec{k}', n} T_\phi(\vec{k}, \vec{k}')$, which is a function of m . **b)** Transfer functions summed over \vec{k}' and m . Note that $T_v(\vec{k}, \vec{k}')$ is multiplied by 20 in both figures to make it visibly different from zero.

Steps 2 and 4 in Fig. 5 come not from the nonconservative linear terms in the equations, but from the conservative nonlinear advective terms. The interactions described by the advective nonlinearities are in the nonlinear transfer functions: $T_j(\vec{k}, \vec{k}')$ in equation 7. It is difficult to study the $T_j(\vec{k}, \vec{k}')$ functions because they are four dimensional functions of (m, n, n', m') , which makes visualization challenging. It is therefore convenient to sum over various transfers or look at specific wavenumber transfers of interest. The most easily decipherable results that compliment the results of Fig. 6 are shown in Fig. 7. First, Fig. 7(a) sums the transfer functions over (n, m', n') , leaving only a function of m , which illustrates the aggregate azimuthal mode number transfers. Note that the sum of each individual curve over m is zero because the nonlinearities are conservative. Positive values in Fig. 7(a) indicate energy transfer into structures with azimuthal mode number m , while negative values indicate energy transfer out of structures with corresponding mode number m . The density and temperature nonlinearities are qualitatively similar in that they cause both forward and inverse transfer out of the wavenumbers that nonconservatively inject the most energy. The potential (polarization) and parallel velocity nonlinearities cause inverse transfer to low wavenumbers.

Figure 7(b) displays the conservative transfers summed over (m, m', n') , leaving only a function of n , which describes transfer into and out of different parallel modes. This is the figure which provides evidence for steps 2 and 4 of the instability diagram. Now, as expected from step 2 of the diagram and foreshadowed by Fig. 6(b), density potential energy is aggregately transferred from $n = 0$ flute modes into $n \neq 0$ modes, specifically $n = \pm 1$. This can be called a direct transfer in analogy with the terminology used for hydrodynamic wavenumber cascades. The temperature fluctuations have the same transfer trends as the density fluctuations, while the parallel velocity exhibits direct transfer, although from $|n| = 1$ to higher modes since there is never any $n = 0$ energy in the parallel velocity. The potential fluctuations, on the other hand, exhibit inverse parallel wavenumber transfer (step 4 of the diagram), populating $n = 0$ potential structures. This nonlinear transfer is the only way to drive energy into $n = 0$ potential structures because $Q_\phi = 0$. That completes the evidence for the nonlinear instability picture along with further details of both the conservative and nonconservative energy dynamics.

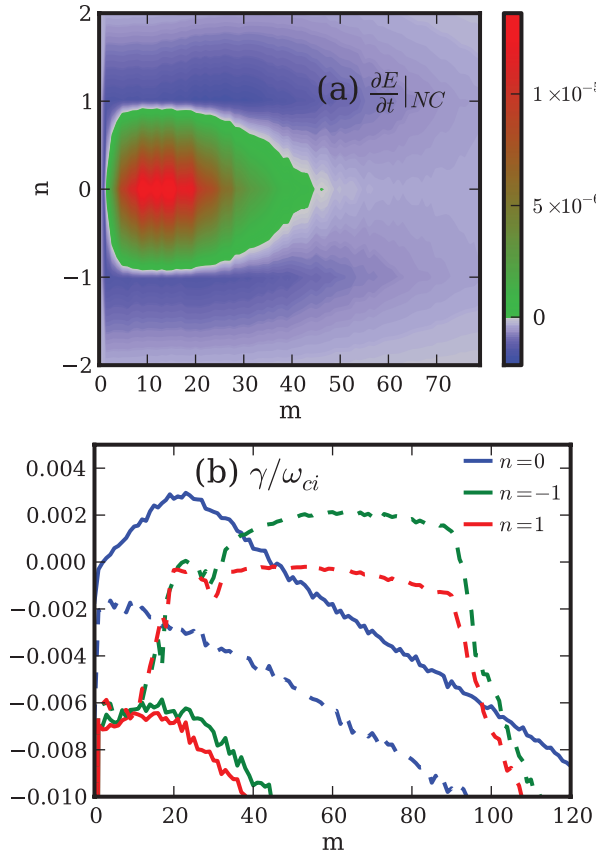


FIG. 8: **a)** The total spectral nonconservative energy injection $\frac{\partial E(\vec{k})}{\partial t}|_{NC}$ and **b)** the spectral nonconservative growth rate spectrum $\gamma_T(\vec{k})$ of the turbulence compared to the linear growth rate spectrum, $\gamma_L(\vec{k})$. The solid lines represent $\gamma_T(\vec{k})$ which is calculated using equation 17 averaged over the saturated turbulent phase, while the dashed lines represent $\gamma_L(\vec{k})$ and are calculated with the same equation using the linear phase of the simulation.

The details of the energy dynamics given above are important but can obscure the most significant results. Specifically, Fig. 6 contains a lot of details that can be contracted by summing over the different energy types. Figure 8 does this, showing the total spectral nonconservative energy dynamics. Figure 8(a), which is a plot of the nonconservative rate of change of the total energy, $\frac{\partial E(\vec{k})}{\partial t}|_{NC} = \sum_j Q_j(\vec{k}) + C_j(\vec{k}) + D_j(\vec{k})$, reveals a global picture in wavenumber space of where the total energy is injected into the system and where it is dissipated. Namely, energy injection occurs on average at $(n = 0, 3 < m < 45)$, while it is dissipated everywhere else including at $n = \pm 1$ for all m . It is obvious that the nonlinear wavenumber transfers must take energy from the injection region to the dissipation region on average, and that is consistent with what was shown in Fig. 7. This further reveals a picture quite different than what one would expect from the standard picture of plasma turbulence in which energy is injected where the *linear* growth rate is positive and dissipated where it is negative. The picture here is quite the opposite – energy is injected where there is no linear instability and dissipated in part where there is one. To clarify this point, the linear growth rate $\gamma_L(\vec{k})$ versus turbulent growth rate $\gamma_T(\vec{k})$ spectra are shown in Fig. 8(b). The growth rates are calculated using:

$$\gamma(\vec{k}) = \left(\sum_j Q_j(\vec{k}) + C_j(\vec{k}) + D_j(\vec{k}) \right) / \left(2 \sum_j E_j(\vec{k}) \right). \quad (17)$$

The turbulent growth rate spectrum, simply means that equation 17 is calculated using the terms from the saturated turbulent phase of the simulation. Note that the linear growth rate is positive for $(n = -1, 35 < m < 95)$ and negative everywhere else. The turbulent growth rate is positive only for $(n = 0, 3 < m < 45)$. The linear and turbulent spectral injection regions do not even overlap. Seemingly, the linear physics is completely washed out in the turbulent state.

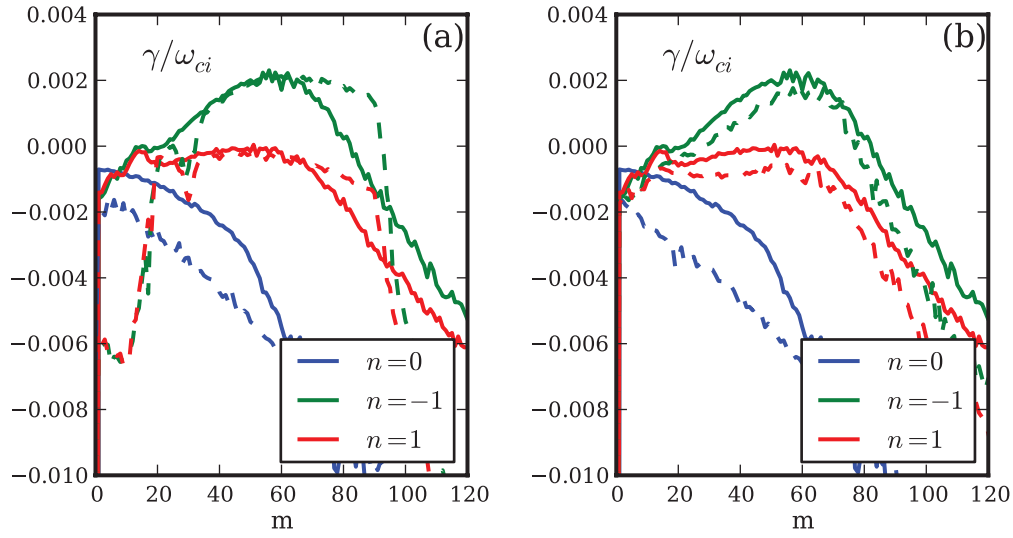


FIG. 9: **a)** The turbulent growth rate spectrum $\gamma_T(\vec{k})$ with $n = 0$ density and potential components removed from the simulation compared to the linear growth rate spectrum $\gamma_L(\vec{k})$. **b)** The solid lines are the same $\gamma_T(\vec{k})$ spectrum as the solid lines in (a), but the dashed lines are the turbulent growth rate spectrum when the zonal flows are retained in the simulation.

Although the nonlinear flute mode dynamics present a clear case of nonlinear instability, the $n \neq 0 \leftrightarrow n = 0$ energy path is not a necessary feature of nonlinear drift wave instabilities, which is clear in tokamak studies of drift wave turbulence [21–25]. Furthermore, the periodic axial boundary conditions used in the LAPD turbulence simulation are obviously unphysical, and more realistic boundary conditions may change the parallel dynamics disallowing an exact $n \neq 0 \leftrightarrow n = 0$ path.

In essence, it is interesting to test the robustness of nonlinear instability in this system. In particular, how important are the idealized flute modes to the nonlinear instability? They are after all, not essential to the otherwise similar nonlinear drift-like instabilities in the tokamak edge simulations [21–25]. Now, there are a few ways to eliminate the flute modes in the simulation such as eliminating one of the nonlinearities that is essential to the nonlinear instability process described in Fig. 5. However, simply subtracting out the $n = 0$ components of the density and potential at each simulation time step retains more of the physics that may be essential to cause nonlinear instability. The energy dynamics of such a simulation, which are succinctly summarized by the growth rate spectrum, are shown in Fig. 9. Interestingly, with no $n = 0$ fluctuations, the turbulent growth rate spectrum $\gamma_T(\vec{k})$ is nearly identical to the linear growth rate spectrum $\gamma_L(\vec{k})$, as seen in Fig. 9(a). It is noted that subtracting out the $n = 0$ potential component removes the zonal flow ($m = n = 0$) from the system, providing a possible explanation for the large change in behavior of the turbulent growth rate spectrum. However, this hypothesis is dispelled by the analysis of a simulation in which only the $n = 0, m \neq 0$ potential components are removed while the zonal flow is left intact. The growth rate spectrum of this simulation, shown in Fig. 9b, reveals that the zonal flow plays a minimal role in the nonlinear instability dynamics. The zonal flow simply decreases the growth rates by a small amount, causing no change to the qualitative picture.

The flute modes are therefore necessary for a nonlinear instability to overtake the linear instability in driving the turbulence, making this qualitatively different from the tokamak edge studies. Furthermore, it is clear from this result that a 2D simplification using a fixed parallel wavelength like the 2D Hasegawa-Wakatani model [38] does not support a nonlinear instability. Nevertheless, one indication that the nonlinear flute-driven instability is important in reproducing experimentally consistent turbulence is that the turbulence of the simulation with the $n = 0$ components removed becomes overly coherent. This can be seen in the frequency spectrum, which is shown in Fig. 10 compared with the experimental spectra and the spectra of the standard nonlinear-instability-dominated simulation. While the standard simulation with the $n = 0$ modes compare well with experimental data, the clear peak in the spectra of the simulation with no $n = 0$ is inconsistent with experiment. This indicates that something in the standard simulation – possibly the nonlinear instability – is important for reproducing experimentally relevant turbulence. A more direct test with realistic axial boundary conditions is left for a future study.

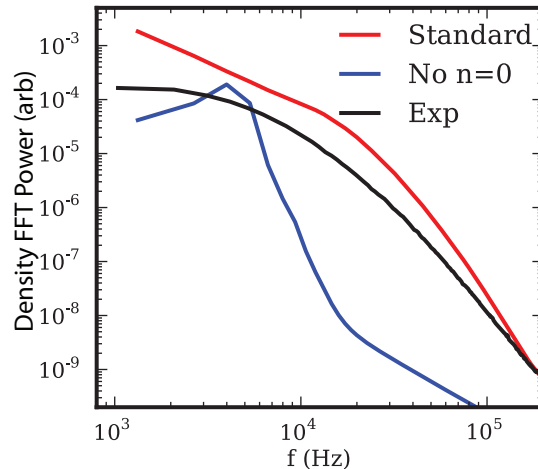


FIG. 10: Comparison of the frequency spectra. Notice the spectra with $n = 0$ components removed is not broadband, but has a clear peak, which is inconsistent with experiment.

VI. CONCLUSION

In contrast to experiments, simulations provide vast quantities of spatial information, and can therefore be useful in illuminating physical processes responsible for driving and saturating turbulence. It is possible to get more than fluctuation levels, flux values, diffusivities, and spectra from simulations. The kind of energy analysis used in this study is one way in which detailed physics can be drawn from a turbulence simulation. Here, energy dynamics analysis shows a complex picture of turbulent energy injection, transfer, and dissipation. Such a picture was certainly not evident *a priori*. Other more advanced procedures such as eigenmode decompositions [1] or proper orthogonal decompositions (POD) [10], which are extensions of this procedure, can reveal even more physical processes, especially those involving saturation.

In this study, a partial spectral decomposition and energy dynamics analysis was sufficient to reveal the dominance of a nonlinear instability in driving and maintaining the turbulence. The nonlinear instability works by driving $k_{\parallel} = 0$ pressure fluctuations using $k_{\parallel} = 0$ pressure and potential fluctuations to access the free energy pressure gradients. The $k_{\parallel} = 0$ potential fluctuations are driven through the finite k_{\parallel} adiabatic response in combination with forward and reverse axial wavenumber transfers. Not only does the nonlinear instability require the $k_{\parallel} = 0 \leftrightarrow k_{\parallel} \neq 0$ transfer path to operate, but the simulation requires this to produce experimentally consistent broadband turbulence. In the future, this study will be expanded to include different and more realistic axial boundary conditions – including conducting plate boundaries – to further test the importance of the flute modes in creating broadband turbulence. Furthermore, different operating conditions in LAPD, including those that produce large mean flows will be simulated and studied to test for the emergence of new dominant instabilities, possibly nonlinear ones.

Understanding nonlinear instabilities is important because they can invalidate the use of quasilinear flux estimates and linear mixing length arguments of turbulent transport levels when linear instabilities are insignificant in the turbulent state. Simple rules for when nonlinear instabilities will act or overtake linear ones are needed, and one attempt at such a rule has been made elsewhere for drift wave turbulence [25]. That rule states that nonlinear instabilities will overtake linear instabilities when $\gamma_L < \omega_*$, which is true for the parameters used in this study. However, more study of this rule and others is warranted, and will be important as long as linear calculations are used to inform predictions of turbulence. Nevertheless, full nonlinear simulations and energy dynamics analyses are most informative and should be used to obtain details of plasma turbulence mechanisms.

Acknowledgments

This research was performed under appointment to the Fusion Energy Sciences Fellowship Program administered by Oak Ridge Institute for Science and Education under a contract between the U.S. Department of Energy and the Oak Ridge Associated Universities. We would also like to thank Paul Terry for many useful discussions on this topic.

The energy evolution for each Fourier mode can be obtained by Fourier decomposing each of equations 1 - 4 and then multiplying the density, electron parallel velocity, vorticity, and electron temperature equations by the complex conjugates of the density, velocity, potential, and temperature respectively, and integrating over space. Adding the resulting equations gives the energy evolution of each Fourier mode.

Take the density equation as an example for this procedure. The decomposition for the density is:

$$N(r, \theta, z, t) = \sum_{\vec{k}} n_{\vec{k}}(r, t) e^{i(m\theta + k_z z)}. \quad (\text{A1})$$

Recall that the subscript \vec{k} is short for (m, n) as the decomposition is a 2D Fourier decomposition in the azimuthal and axial directions, making the sum over \vec{k} truly a double sum over m and n . Furthermore, positive and negative m and n are included in the sums to ensure reality of N , which also requires that $n_{-\vec{k}} = n_{\vec{k}}^*$. Similar decompositions are used for $v_{\parallel e}$ and ϕ . The density source is azimuthally symmetric, so it is decomposed as:

$$S_N(r, z, t) = \sum_{k_z} S_{Nk_z}(r, t) e^{ik_z z}. \quad (\text{A2})$$

Substituting this decomposition into equation 1 gives:

$$\begin{aligned} \sum_{\vec{k}} \frac{\partial n_{\vec{k}}}{\partial t} e^{i(m\theta + k_z z)} &= \sum_{k_z} S_{Nk_z} e^{ik_z z} + \\ \sum_{\vec{k}} \left[-\frac{im}{r} \partial_r N_0 \phi_{\vec{k}} - ik_z N_0 v_{\vec{k}} + \mu_N (\partial_r^2 n_{\vec{k}} + \frac{1}{r} \partial_r n_{\vec{k}} - \frac{m^2}{r^2} n_{\vec{k}}) \right] e^{i(m\theta + k_z z)} \\ &+ \frac{1}{r} \sum_{\vec{k}, \vec{k}'} (im n_{\vec{k}} \partial_r \phi_{\vec{k}'} - im' \partial_r n_{\vec{k}} \phi_{\vec{k}'}) e^{i(m+m')\theta + i(k_z + k'_z)z}. \end{aligned} \quad (\text{A3})$$

Multiplying through by $n_{\vec{k}}^* e^{-im'\theta - ik'_z z}$ and integrating over space (and permuting primes) gives:

$$\begin{aligned} \left\langle \frac{\partial n_{\vec{k}}}{\partial t} n_{\vec{k}}^* \right\rangle &= \langle S_{Nk_z} n_{m=0, k_z}^* \rangle \\ \left\langle -\frac{im}{r} \partial_r N_0 \phi_{\vec{k}} n_{\vec{k}}^* - ik_z N_0 v_{\vec{k}} n_{\vec{k}}^* + \mu_N (\partial_r^2 n_{\vec{k}} + \frac{1}{r} \partial_r n_{\vec{k}} - \frac{m^2}{r^2} n_{\vec{k}}) n_{\vec{k}}^* \right\rangle \\ &+ \left\langle \frac{1}{r} \sum_{\vec{k}'} (im' n_{\vec{k}} \partial_r \phi_{\vec{k}-\vec{k}'} n_{\vec{k}}^* - i(m-m') \partial_r n_{\vec{k}'} \phi_{\vec{k}-\vec{k}'} n_{\vec{k}}^*) \right\rangle. \end{aligned} \quad (\text{A4})$$

Finally, taking the real part of this equation results in:

$$\begin{aligned} \left\langle \frac{1}{2} \frac{\partial |n_{\vec{k}}|^2}{\partial t} \right\rangle &= \text{Re} \{ \langle S_{Nk_z} n_{m=0, k_z}^* \rangle \} \\ \text{Re} \left\{ \left\langle -\frac{im}{r} \partial_r N_0 \phi_{\vec{k}} n_{\vec{k}}^* - ik_z N_0 v_{\vec{k}} n_{\vec{k}}^* + \mu_N (\partial_r^2 n_{\vec{k}} + \frac{1}{r} \partial_r n_{\vec{k}} - \frac{m^2}{r^2} n_{\vec{k}}) n_{\vec{k}}^* \right\rangle \right\} \\ &+ \text{Re} \left\{ \left\langle \frac{1}{r} \sum_{\vec{k}'} (im' n_{\vec{k}} \partial_r \phi_{\vec{k}-\vec{k}'} n_{\vec{k}}^* - i(m-m') \partial_r n_{\vec{k}'} \phi_{\vec{k}-\vec{k}'} n_{\vec{k}}^*) \right\rangle \right\}. \end{aligned} \quad (\text{A5})$$

Note that taking the real part of the equation produces the expected energy-like term on the left hand side because:

$$\frac{1}{2} \frac{\partial |n_{\vec{k}}|^2}{\partial t} = \text{Re} \left\{ \frac{\partial n_{\vec{k}}}{\partial t} n_{\vec{k}}^* \right\}. \quad (\text{A6})$$

Breaking the result into explicit parts:

$$\frac{\partial E_n(\vec{k})}{\partial t} = Q_n(\vec{k}) + C_n(\vec{k}) + D_n(\vec{k}) + \sum_{\vec{k}'} T_n(\vec{k}, \vec{k}') \quad (\text{A7})$$

$$E_n(\vec{k}) = \frac{1}{2} \langle |n_{\vec{k}}|^2 \rangle \quad (\text{A8})$$

$$Q_n(\vec{k}) = \text{Re} \left\{ \left\langle -\frac{im}{r} \partial_r N_0 \phi_{\vec{k}} n_{\vec{k}}^* \right\rangle \right\} \quad (\text{A9})$$

$$C_n(\vec{k}) = \text{Re} \left\{ \left\langle -ik_z N_0 v_{\vec{k}} n_{\vec{k}}^* \right\rangle \right\} \quad (\text{A10})$$

$$D_n(\vec{k}) = \text{Re} \left\{ \left\langle \mu_N (\partial_r^2 n_{\vec{k}} + \frac{1}{r} \partial_r n_{\vec{k}} - \frac{m^2}{r^2} n_{\vec{k}}) n_{\vec{k}}^* + S_{Nk_z} n_{m=0, k_z}^* \right\rangle \right\} \quad (\text{A11})$$

$$T_n(\vec{k}, \vec{k}') = \text{Re} \left\{ \left\langle \frac{1}{r} \left(im' n_{\vec{k}'} \partial_r \phi_{\vec{k}-\vec{k}'} n_{\vec{k}}^* - i(m-m') \partial_r n_{\vec{k}'} \phi_{\vec{k}-\vec{k}'} n_{\vec{k}}^* \right) \right\rangle \right\} \quad (\text{A12})$$

$Q_n(\vec{k})$ is the energy injection, $C_n(\vec{k})$ is the transfer channel, $D_n(\vec{k})$ is dissipation, and $T_n(\vec{k}, \vec{k}')$ is spectral energy transfer. The same type of procedure may be applied to equations 2-4. However, the double primed conjugate multiplications (as in the step between equations A3 and A4) must be done with the Fourier fields, $\frac{m_e}{m_i} v_{\vec{k}''}$, $-\phi_{\vec{k}''}$, and $\frac{3}{2} t_{\vec{k}''}$, rather than $v_{\vec{k}''}$, $\varpi_{\vec{k}''}$, and $t_{\vec{k}''}$. These produce the correct energy terms, and most importantly still conserve the nonlinearities. The corresponding expressions for the perpendicular kinetic energy are:

$$\frac{\partial E_\phi(\vec{k})}{\partial t} = Q_\phi(\vec{k}) + C_\phi(\vec{k}) + D_\phi(\vec{k}) + \sum_{\vec{k}'} T_\phi(\vec{k}, \vec{k}') \quad (\text{A13})$$

$$E_\phi(\vec{k}) = \frac{1}{2} \left\langle N_0 \left| \frac{\partial \phi_{\vec{k}}}{\partial r} \right|^2 + N_0 \frac{m^2}{r^2} |\phi_{\vec{k}}|^2 \right\rangle \quad (\text{A14})$$

$$Q_\phi(\vec{k}) = 0 \quad (\text{A15})$$

$$C_\phi(\vec{k}) = \text{Re} \left\{ \left\langle ik_z N_0 v_{\vec{k}} \phi_{\vec{k}}^* \right\rangle \right\} \quad (\text{A16})$$

$$D_\phi(\vec{k}) = \text{Re} \left\{ \left\langle -\mu_\phi (\partial_r^2 \varpi_{\vec{k}} + \frac{1}{r} \partial_r \varpi_{\vec{k}} - \frac{m^2}{r^2} \varpi_{\vec{k}}) \phi_{\vec{k}}^* - \nu_{in} E_\phi(\vec{k}) \right\rangle \right\} \quad (\text{A17})$$

$$T_\phi(\vec{k}, \vec{k}') = \text{Re} \left\{ \left\langle -\frac{1}{r} \left(im' \varpi_{\vec{k}'} \partial_r \phi_{\vec{k}-\vec{k}'} \phi_{\vec{k}}^* - i(m-m') \partial_r \varpi_{\vec{k}'} \phi_{\vec{k}-\vec{k}'} \phi_{\vec{k}}^* \right) \right\rangle \right\} \quad (\text{A18})$$

and for the electron temperature potential energy:

$$\frac{\partial E_t(\vec{k})}{\partial t} = Q_t(\vec{k}) + C_t(\vec{k}) + D_t(\vec{k}) + \sum_{\vec{k}'} T_t(\vec{k}, \vec{k}') \quad (\text{A19})$$

$$E_t(\vec{k}) = \frac{3}{4} \langle |t_{\vec{k}}|^2 \rangle \quad (\text{A20})$$

$$Q_t(\vec{k}) = \text{Re} \left\{ \left\langle -\frac{3im}{2r} \partial_r T_{e0} \phi_{\vec{k}} t_{\vec{k}}^* \right\rangle \right\} \quad (\text{A21})$$

$$C_t(\vec{k}) = \text{Re} \left\{ \left\langle -1.71 ik_z T_{e0} v_{\vec{k}} t_{\vec{k}}^* \right\rangle \right\} \quad (\text{A22})$$

$$D_t(\vec{k}) = \text{Re} \left\{ \left\langle -\frac{\kappa_{||e}}{N_0} k_z^2 |t_{\vec{k}}|^2 - \frac{3m_e}{m_i} \nu_e |t_{\vec{k}}|^2 + \frac{3}{2} \mu_T (\partial_r^2 t_{\vec{k}} + \frac{1}{r} \partial_r t_{\vec{k}} - \frac{m^2}{r^2} t_{\vec{k}}) t_{\vec{k}}^* + \frac{3}{2} S_{Tk_z} t_{m=0, k_z}^* \right\rangle \right\} \quad (\text{A23})$$

$$T_t(\vec{k}, \vec{k}') = \text{Re} \left\{ \left\langle \frac{3}{2r} \left(im' t_{\vec{k}'} \partial_r \phi_{\vec{k}-\vec{k}'} t_{\vec{k}}^* - i(m-m') \partial_r t_{\vec{k}'} \phi_{\vec{k}-\vec{k}'} t_{\vec{k}}^* \right) \right\rangle \right\} \quad (\text{A24})$$

and for the parallel kinetic energy:

$$\frac{\partial E_v(\vec{k})}{\partial t} = Q_v(\vec{k}) + C_v(\vec{k}) + D_v(\vec{k}) + \sum_{\vec{k}'} T_v(\vec{k}, \vec{k}') \quad (\text{A25})$$

$$E_v(\vec{k}) = \frac{1}{2} \frac{m_e}{m_i} \langle |v_{\vec{k}}|^2 \rangle \quad (\text{A26})$$

$$Q_v(\vec{k}) = \text{Re} \left\{ \left\langle ik_z \frac{N_0^2 - T_{e0}}{N_0} n_{\vec{k}} v_{\vec{k}}^* + ik_z (1 - N_0) \phi_{\vec{k}} v_{\vec{k}}^* + 1.71 ik_z (T_{e0} - 1) t_{\vec{k}} v_{\vec{k}}^* \right\rangle \right\} \quad (\text{A27})$$

$$C_v(\vec{k}) = \text{Re} \left\{ \left\langle -ik_z N_0 n_{\vec{k}} v_{\vec{k}}^* + ik_z N_0 \phi_{\vec{k}} v_{\vec{k}}^* - 1.71 ik_z T_{e0} t_{\vec{k}} v_{\vec{k}}^* \right\rangle \right\} \quad (\text{A28})$$

$$D_v(\vec{k}) = \text{Re} \left\{ \left\langle -\nu_e \frac{m_e}{m_i} |v_{\vec{k}}|^2 \right\rangle \right\} \quad (\text{A29})$$

$$T_v(\vec{k}, \vec{k}') = \text{Re} \left\{ \frac{m_e}{m_i} \left\langle \frac{1}{r} \left(im' v_{\vec{k}'} \partial_r \phi_{\vec{k}-\vec{k}'} v_{\vec{k}}^* - i(m - m') \partial_r v_{\vec{k}'} \phi_{\vec{k}-\vec{k}'} v_{\vec{k}}^* \right) \right\rangle \right\} \quad (\text{A30})$$

The transfer channel $C_v(\vec{k})$ is specifically set so that $C_n(\vec{k}) + C_t(\vec{k}) + C_\phi(\vec{k}) + C_v(\vec{k}) = 0$. The source $Q_v(\vec{k})$ is the left over quantity, which can have any sign and contributes to the overall energy evolution.

-
- [1] D.A. Baver, P.W. Terry, R. Gatto, and Eduardo Fernandez. Nonlinear stability and instability in collisionless trapped electron mode turbulence. *Phys. Plasmas*, 9:3318, 2002.
 - [2] P.W. Terry, R. Gatto, and D.A. Baver. Nonlinear damping of plasma zonal flows excited by inverse spectral transfer. *Phys. Rev. Lett.*, 89:205001, 2002.
 - [3] P.W. Terry and R. Gatto. Nonlinear inward particle flux component in trapped electron mode turbulence. *Phys. Plasmas*, 13:062309, 2006.
 - [4] P.W. Terry, D.A. Baver, and Sangeeta Gupta. Role of stable eigenmodes in saturated local plasma turbulence. *Phys. Plasmas*, 13:022307, 2006.
 - [5] R. Gatto, P.W. Terry, and D.A. Baver. Nonlinear damping of zonal modes in anisotropic weakly collisional trapped electron mode turbulence. *Phys. Plasmas*, 13:022306, 2006.
 - [6] P.W. Terry, D.A. Baver, and D.R. Hatch. Reduction of inward momentum flux by damped eigenmodes. *Phys. Plasmas*, 16:122305, 2009.
 - [7] D.R. Hatch, P.W. Terry, W.M. Nevins, and W. Dorland. Role of stable eigenmodes in gyrokinetic models of ion temperature gradient turbulence. *Phys. Plasmas*, 16:022311, 2009.
 - [8] J.-H. Kim and P.W. Terry. Energetic study of the transition to nonlinear state in two-dimensional electron temperature gradient fluid turbulence. *Phys. Plasmas*, 17:112306, 2010.
 - [9] K.D. Makwana, P.W. Terry, J.-H. Kim, and D.R. Hatch. Damped eigenmode saturation in plasma fluid turbulence. *Phys. Plasmas*, 18:012302, 2011.
 - [10] D.R. Hatch, P.W. Terry, F. Jenko, F. Merz, and W.M. Nevins. Saturation of gyrokinetic turbulence through damped eigenmodes. *Phys. Rev. Lett.*, 106:115003, 2011.
 - [11] A. N. Kolmogorov. The local structure of turbulence in incompressible viscous fluid for very large reynolds numbers. *Dokl Akad. Nauk SSSR*, 30:301–305, 1941.
 - [12] S.J. Camargo, M.K. Tippet, and I.L. Caldas. Nonmodal energetics of resistive drift waves. *Phys. Rev. E*, 58:3693, 1998.
 - [13] P. Manneville. Understanding the sub-critical transition to turbulence in wall flows. *Pramana*, 70:1009–1021, 2008.
 - [14] B. D. Scott. Self-sustained collisional drift-wave turbulence in a sheared magnetic field. *Phys. Rev. Lett.*, 65:3289, 1990.
 - [15] B. D. Scott. The mechanism of self sustainment in collisional drift wave turbulence. *Phys. Fluids B*, 4:2468, 1992.
 - [16] J.F. Drake, A. Zeiler, and D. Biskamp. Nonlinear self-sustained drift-wave turbulence. *Phys. Rev. Lett.*, 75:4222, 1995.
 - [17] H. Nordman, V.P. Pavlenko, and J. Weiland. Subcritical reactive drift wave turbulence. *Phys. Fluids B*, 5:402, 1993.
 - [18] R.E. Waltz. Subcritical magnetohydrodynamic turbulence. *Phys. Rev. Lett.*, 55:1098, 1985.
 - [19] K. Itoh, S.I. Itoh, M. Yagi, and A. Fukuyama. Subcritical excitation of plasma turbulence. *Journal of the Physical Society of Japan*, 65:2749–2752, 1996.
 - [20] E. G. Highcock, A. A. Schekochihin, S. C. Cowley, M. Barnes, F. I. Parra, C. M. Roach, and W. Dorland. Zero-turbulence manifold in a toroidal plasma. *Phys. Rev. Lett.*, submitted.
 - [21] A. Zeiler, D. Biskamp, J.F. Drake, and P.N. Guzdar. Three-dimensional fluid simulations of tokamak edge turbulence. *Phys. Plasmas*, 3:2951, 1996.
 - [22] A. Zeiler, J.F. Drake, and D. Biskamp. Electron temperature fluctuations in drift-resistive ballooning turbulence. *Phys. Plasmas*, 4:991, 1997.

- [23] B. D. Scott. The nonlinear drift wave instability and its role in tokamak edge turbulence. *New J. Physics*, 4:52.1–52.30, 2002.
- [24] B. D. Scott. Computation of electromagnetic turbulence and anomalous transport mechanisms in tokamak plasmas. *Plasma Phys. Control. Fusion*, 45:A385–A398, 2003.
- [25] B. D. Scott. Drift wave versus interchange turbulence in tokamak geometry: Linear versus nonlinear mode structure. *Phys. Plasmas*, 12:062314, 2005.
- [26] D. Biskamp and A. Zeiler. Nonlinear instability mechanism in 3d collisional drift-wave turbulence. *Phys. Rev. Lett.*, 74:706, 1995.
- [27] S. B. Korsholm, P. K. Michelsen, and V. Naulin. Resistive drift wave turbulence in a three-dimensional geometry. *Phys. Plasmas*, 6:2401, 1999.
- [28] A.M. Dimits, G. Bateman, and et. al. Comparisons and physics basis of tokamak transport models and turbulence simulations. *Phys. Plasmas*, 7:969, 2000.
- [29] D.R. Ernst, P.T. Bonoli, and et. al. Role of trapped electron mode turbulence in internal transport barrier control in the alcator c-mod tokamak. *Phys. Plasmas*, 11:2637, 2004.
- [30] S I Braginskii. Transport processes in a plasma. In M A Leontovich, editor, *Reviews of Plasma Physics*, volume 1, pages 205–311. Consultants Bureau, New York, 1965.
- [31] B. D. Dudson, M. V. Umansky, X. Q. Xu, P. B. Snyder, and H. R. Wilson. Bout++: A framework for parallel plasma fluid simulations. *Computer Physics Communications*, pages 1467–1480, 2009.
- [32] P. Popovich, M.V. Umansky, T. A. Carter, and B. Friedman. Analysis of plasma instabilities and verification of bout code for linear plasma device. *Phys. Plasmas*, 17:102107, 2010.
- [33] P. Popovich, M.V. Umansky, T. A. Carter, and B. Friedman. Modeling of plasma turbulence and transport in the large plasma device. *Phys. Plasmas*, 17:122312, 2010.
- [34] M.V. Umansky, P. Popovich, T. A. Carter, B. Friedman, and W.M. Nevins. Numerical simulation and analysis of plasma turbulence the large plasma device. *Phys. Plasmas*, 18:055709, 2011.
- [35] B. Friedman, M.V. Umansky, and T.A. Carter. Grid convergence study in a simulation of lapd turbulence. *Contrib. Plasma Phys.*, 52:412–416, 2012.
- [36] A. Arakawa. Computational design for long-term numerical integration of the equations of fluid motion. *J. Computational Physics*, 1:119–143, 1966.
- [37] B. Rogers and P. Ricci. Low-frequency turbulence in a linear magnetized plasma. *Phys. Rev. Lett.*, 104:225002, 2010.
- [38] A. Hasegawa and M. Wakatani. Plasma edge turbulence. *Phys. Rev. Lett.*, 50:682–686, 1983.